Flight dynamic modeling and stability of a small-scale side-by-side helicopter for Urban Air Mobility

Flight dynamic modeling and stability of a small-scale side-by-side helicopter for Urban Air Mobility

Francesco Mazzeo[a,1,*], Marilena D.Pavel[b,1], Daniele Fattizzo[c,1], Giulia Bertolani[c,1], Emanuele L. de Angelis[c,1], Fabrizio Giulietti[c,1]

[a] *University of Modena and Reggio Emilia, Department of Engineering, Modena, Italy 47121*
[b] *Delft University of Technology, Faculty of Aerospace Engineering, Department of Simulation and Control, Delft, The Netherlands, 2629HS*
[c] *University of Bologna, Department of Industrial Engineering, CIRI Aerospace, Forlí, Italy 47121*

Abstract

This paper aims to explore the development of a flight dynamics model for a small-scale side-by-side helicopter and describe its trim and stability characteristics. The helicopter is considered a suitable candidate for Urban Air Mobility (UAM) solutions, because of its reliable design and low noise characteristics, but still very small knowledge is present on the mathematical modeling approaches and dynamic properties. A 14 degrees of freedom nonlinear mathematical model is developed and semi-analytical models are employed to account for the presence of the shrouds. An iterative trim routine is developed and applied with a suitable control mix that allows the use of classic helicopter controls. To control the vertical speed and roll rate, the paper assumes an equal collective pitch and lateral cyclic in the two

*Corresponding author
[1]Ph.D. Student, francesco.mazzeo@unimore.it

rotors, while a uniform plus a differential longitudinal cyclic is adopted for pitch and yaw maneuvers. The paper discusses unique characteristics of the side-by-side configuration as obtained from the stability analysis: an unstable high-frequency mode, governed by the vertical velocity and pitch angle arises when the center of gravity (CG) of the vehicle is aligned or placed in front of the two main rotors. Similarly, both lateral phugoid and roll subsidence modes are sensitive to the CG location. The side-by-side configuration presents also a stable spiral mode which needs to be carefully designed.
Keywords: Flight Dynamics, helicopter, side-by-side, Urban Air Mobility, stability, trim

---

Nomenclature

$\boldsymbol{a} = [a_0\ a_1\ b_1]$	Vector of tip-path plane (TPP) coordinates, thus coning angle (a_0), longitudinal (a_1) and lateral (b_1) disc tilt angles
A	State matrix
a_w	Wake contraction factor due to shrouds
B	Control matrix
c	Chord
C_L, C_D	Blade lift and drag coefficients
C_{L_s}, C_{D_s}	Blade lift and drag coefficients at stall angle of attack
C_{L_α}	Lift coefficient curve's slope in pre-stall region

C_D^f, C_D^s, C_D^t	Fuselage's parasite drag coefficients
$C_T = \frac{T_r}{\rho\pi R^2(\Omega R)^2}$	Rotor thrust coefficient
D	Fuselage drag
$\tilde{D}$, $\tilde{k}$, $\tilde{f}$	TPP dynamic equation coefficients
e	Hinge offset
$\boldsymbol{F} = [X\ Y\ Z]$	Sum of external forces (aerodynamics, fuselage and inertial)
$\boldsymbol{F_a}$, $\boldsymbol{F_i}$, $\boldsymbol{F_g}$, $\boldsymbol{F_f}$	Respectively: aerodynamic, inertial, gravitational and fuselage force in body f.o.r.
g	Acceleration of gravity
$[H_w\ Y_w\ T_r]$	Aerodynamic force in the hub-wind frame of reference (horizontal, lateral and thrust)
I	Rotorcraft Inertia matrix
I_{xx}, I_{yy}, I_{zz}	Inertia moment wrt x_B, y_B and z_B axes
I_{yz}, I_{xz}, I_{xy}	Inertia product wrt x_B, y_B and z_B axes
K_b	Spring restraint coefficient due to flap
K_v	Velocity ratio between the inlet and the outlet of the shorud
k_{C_L}	Lift coefficient curve's correction factor, according to Viterna model
$[L_w\ M_w\ Q]$	Aerodynamic moment in the hub-wind frame of reference (rolling, pitching and torque)

1	m_{to}	Maximum take-off mass
2	m_b	Blade mass
3	$\boldsymbol{M} = [L\ M\ N]$	Sum of external moments (aerodynamics, fuselage and inertial)
4	$\boldsymbol{M_a}$, $\boldsymbol{M_i}$, $\boldsymbol{M_f}$	Respectively: aerodynamic, inertial, and fuselage moment
5	N_b	Number of blades
6	$\boldsymbol{r_H}$	Hub position wrt body axes frame of reference
7	$\boldsymbol{r_{CP}}$	Center of Pressure position wrt body axes frame of reference
8	r_k	Duct lip radius
9	R	Rotor radius
10	S^f, S^s, S^t	Equivalent fuselage surfaces
11	T	Main rotor total thrust
12	T_d	Rotor thrust due to shroud
13	T_d	Rotor thrust due to rotor
14	$\boldsymbol{U_B} = [u\ v\ w]$	Relative wind velocity expressed in body axes frame of reference
15	$\boldsymbol{U_H} = [u_H\ v_H\ w_H]$	Relative wind velocity expressed in hub-body axes frame of reference
16	$U_\infty = \lvert\boldsymbol{U_B}\rvert$	Wind velocity magnitude

$\hat{\boldsymbol{U}} = \boldsymbol{U_B}/U_\infty$	Unit vector aligned with the incoming flow velocity
v_i	Induced inflow velocity
x	State vector
$\hat{\boldsymbol{x}}$, $\hat{\boldsymbol{y}}$, $\hat{\boldsymbol{z}}$	Unit vectors perpendicular to the frontal, side and top faces
$[x_B\ y_B\ z_B]$	Body axes frame of reference (f.o.r.): right-handed axes system, centered on the rotorcraft center of gravity, x_B pointing towards the nose of the vehicle, and the y_B pointing towards the right-hand side main rotor
$[x_H\ y_H\ z_H]$	Hub-Body axes frame of reference: centered on the main rotor center of rotation, with the x_H and z_H axes respectively perpendicular and parallel to the shaft and y_H pointing towards the rotorcraft CG
$[x_G\ y_G\ z_G]$	Center of gravity (CG) coordinates in body axes f.o.r.
Greek symbols	
α	Blade's angle of attack
α_s	Blade's angle of attack
β	Blade's flapping angle

$\beta_w = \text{atan}_2(v_H, u_H)$	Sideslip angle of the rotor
Γ	Rotor sense of rotation (-1 for clockwise, 1 for counterclockwise)
δx	General small perturbation
δ	Blade's tip clearance
$\delta_f = 1 - 109\frac{\delta}{R}\sqrt{\frac{\delta}{R}}$	Blade's tip clearance factor
$\lambda_i = \frac{v_i}{\Omega R}$	Induced inflow ratio
$\lambda = \lambda_i + \frac{w_H}{\Omega R}$	Total inflow ratio
$\mu = \frac{\sqrt{u_H^2 + v_H^2}}{\Omega R}$	Rotor advance ratio
ξ_{in}, ξ_{out}	Inlet and outlet drag factor of the shroud
σ	Solidity ratio
τ	Control vector
$[\phi\ \theta\ \psi]$	Euler's angles (roll, pitch, yaw)
ψ_b	Blade's azimuthal position
Ω	Rotor angular velocity
$\boldsymbol{\omega}_H$	Angular velocity in hub-body f.o.r.
$\boldsymbol{\omega}_B = [p\ q\ r]$	Angular velocity in body axes f.o.r.

Rotor Controls

θ_0	Collective pitch control
A_{1s}	Lateral cyclic control
B_{1s}	Longitudinal cyclic control
ΔB_{1s}	Differential longitudinal cyclic control

1. Introduction

In 2022, the transport industry was responsible for more than 20% of the global greenhouse gas emissions, whose majority can be related to road transport and aviation sectors (2022 IEA report [1, 2]). The alarming increase of CO_2 production in the last decades has led to the definition of innovative, green-oriented, transport solutions. UAM is an example of a sustainable industry sector that has solidly grown in the last few years with the aim of moving part of classical urban and regional transport into the third dimension [3, 4, 5, 6]. The main characters of UAM are the Vertical Take-Off and Landing (VTOL) aircraft, which can be employed in a typical ecosystem to perform services such as air taxi, last-mile delivery, rescue, and emergency transportation within urban and regional environments. A large variety of VTOL configurations has been designed and investigated in order to find the most suitable arrangement for particular scenarios. Silva and Johnson proposed performance studies and sizing methodologies for VTOLs [7, 8], setting the stage for future developments of each configuration. Multirotors [9, 10, 11], tilt-rotors [12, 13, 14, 15], lift+cruise [16] platforms and helicopters are some of the most investigated solutions [17].

A classic example of a dual-rotor helicopter developed in the past corresponds to the tandem configuration. One of the most famous models is the Boeing CH-47 Chinhook developed in the 60s for the U.S. Army. Several studies can be found in the literature related to this vehicle, both from an experimental [18, 19, 20] and a numerical standpoint [21, 22, 23]. Although

this configuration is highly accepted as a proper solution for a wide range of operations, particularly in heavy-weight lifting, it is known that it presents some criticalities related to the stability and aerodynamic properties of the two rotors. According to Newman [24], the presence of aft and rear rotors may induce potential mode couplings between longitudinal and lateral dynamics that can be detrimental to the rotorcraft controllability. In addition, when the rotorcraft assumes a nose-up attitude during landing operations, the rear rotor may operate directly in the downwash of the aft one and induce pitch instability. A solution to reduce this effect can be found by rearranging the rotors side-by-side, with the longitudinal axis perpendicular to the rotor-rotor one.

In this paper, a small-scale side-by-side helicopter available at the University of Bologna is presented and studied. The rotorcraft has two ducted, counter-rotating rotors placed outside of the fuselage's boundary, with zero overlap and negligible aerodynamic interaction with the airframe [25, 26]. The presence of the ducts makes the rotorcraft suitable to operate within urban environments, increases the level of safety and societal acceptance [27] and provides a beneficial effect on the overall noise generated by the rotors [28]. Indeed, a potential drawback of this configuration is the noise generated by the aerodynamic interaction of the rotors with the fuselage and the rotors themselves. As a matter of fact, most of the side-by-side helicopters studied in the literature, present two overlapped and intermeshing rotors. An acoustic prediction of the background noise generated by side-by-side ro-

tors in hovering conditions, with different levels of overlap, was conducted by Sagaga *et al.* [29] by employing numerical simulations. It was found that the noise level, which is mainly related to the tip vortex interactions between the two rotors, can be decreased by reducing the level of overlap between the two rotors. Nevertheless, the rumor intensity still remained above the maximum threshold set by Uber for air taxi services in a UAM ecosystem (67 dB at 500 ft altitude [30]). As a matter of fact, while the majority of the research efforts have been focused on alternative configurations or acoustic predictions of the side-by-side helicopter noise [31, 32], very small knowledge is still present on the flight dynamic properties of this particular configuration. A simplified numerical model, based on blade element theory, was presented by Rao *et al.* [33] to design an attitude feedback control for this type of aircraft. However, the trim and stability qualities of the VTOL were not fully assessed and detailed research addressing the equilibrium, stability, and dynamic features of such configuration is not yet available. The scope of this paper is thus to fill in this gap by developing an advanced numerical model of the above-mentioned small-scale eVTOL, with the aim to provide the flight dynamics community a reliable tool for studying the trim and stability of future UAM platforms. Contributions of this article to the state of the art can be summarized as follows:

1. A full 14 DoF nonlinear mathematical model, with accurate modeling of all rotor dynamics features

2. Development of a trim procedure and linear state-space model

3. Dynamic modes analysis and detailed discussion of aircraft dynamic behavior in relation to flight condition and relevant design parameters.

The present paper is organized as follows. In Section 2 the case study is presented and a description of the particular configuration and controlling methods is given. Section 3 outlines the modeling framework, while in Section 4, the trim conditions of the rotorcraft are investigated by employing an iterative algorithm. In Section 5, the linearized mathematical model is described and the main modes are presented. Finally, Section 6 discusses the main outcomes from this study while Section 7 reports the concluding remarks.

2. Design overview

The case study is a small-scale electric dual-rotor VTOL configuration produced by SAB Group S.R.L. The rotorcraft is composed of two identical semirigid helicopter rotors according to a side-by-side arrangement and connected by a carbon fiber beam with no incidence angle. The fuselage is a lightweight carbon fiber structure, symmetric with respect to the plane $x_B - z_B$ (Figure 1), and designed to allocate two 22000 mAh Li-Po batteries underneath. Two custom-made electric motors are placed at the very end parts of the upper beam. The shrouded rotors are synchronous and counter-rotating and they operate at constant angular speed. Figure 1 illustrates the design, while the technical specifications are reported in Table 1.

In particular, the main rotor 1 (MR1) is referred to as the right-hand side clockwise rotor, while the main rotor 2 (MR2) is referred to as the left-hand side counterclockwise rotor.

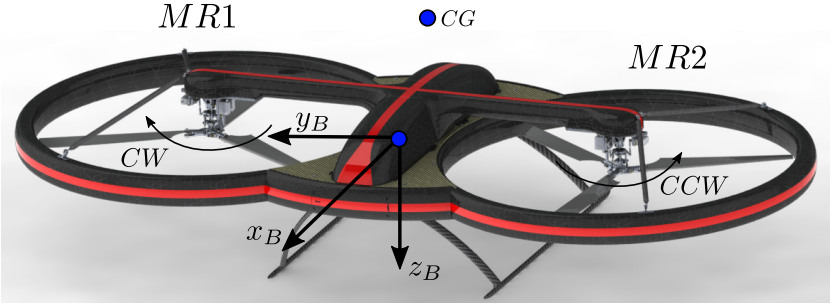

Figure 1: Electric dual-rotor VTOL configuration, courtesy of SAB Group S.R.L.

Description	Symbol	Value
Maximum Take-Off Mass [kg]	m_{to}	20.62
Inertia moment wrt x_B [kgm^2]	I_{xx}	3.532
Inertia moment wrt y_B [kgm^2]	I_{yy}	2.222
Inertia moment wrt z_B [kgm^2]	I_{zz}	5.342
Inertia product wrt x_B [kgm^2]	I_{yz}	0
Inertia product wrt y_B [kgm^2]	I_{xz}	-0.052
Inertia product wrt z_B [kgm^2]	I_{xy}	-0.001
Rotors (same design, counterrotating)		
Sense of rotation	Γ	$\pm$ 1
Number of blades	N_b	3
Radius [m]	R	0.505
Mean Chord [m]	c	0.051
Solidity ratio [-]	σ	0.0964
Angular velocity [rpm]	Ω	2400
Hinge offset [m]	e	0.075
Blade mass [kg]	m_b	0.2875
Spring restraint coefficient due to flap [Nm/rad]	K_b	162
Hub position of the MR1 wrt body axes [m]	$\boldsymbol{r}_H^{(1)}$	[0 -0.645 0.066]
Hub position of the MR2 wrt body axes [m]	$\boldsymbol{r}_H^{(2)}$	[0 0.645 0.066]

Table 1: Rotorcraft technical specifications.

Each rotor is equipped with the conventional helicopter controls, i.e. collective ($\theta_0^{(1,2)}$), longitudinal cyclic ($B_{1s}^{(1,2)}$), and lateral cyclic ($A_{1s}^{(1,2)}$), where the superscripts $^{(1)}$ and $^{(2)}$ refer respectively to the MR1 and MR2. The rotorcraft is over-actuated, meaning that the set of six controls requires proper mixing to reduce it to four independent controls [34]. The global collective pitch (θ_0) is used to control the vehicle along the vertical axis, while global lateral and longitudinal cyclic (A_{1s} and B_{1s}, respectively) allows for controlling the roll and pitch attitude. The heading angle control is introduced by a differential longitudinal cyclic ΔB_{1s}. Lateral and forward movements are performed with a simultaneous modification of the single longitudinal and lateral controls, as well as the collective pitch, which is kept equal in the two rotors. Summarizing, the vertical motion is controlled by the collective pitch $\theta_0 = \theta_0^{(1)} = \theta_0^{(2)}$, roll and pitch axes are controlled by the lateral and longitudinal cyclic, respectively:

$$A_{1s} = A_{1s}^{(1)} = A_{1s}^{(2)} \qquad \text{and} \qquad B_{1s} = \frac{B_{1s}^{(1)} + B_{1s}^{(2)}}{2} \tag{1}$$

whereas the yaw axis is controlled by

$$\Delta B_{1s} = \frac{B_{1s}^{(2)} - B_{1s}^{(1)}}{2} \tag{2}$$

In such a way, the rotorcraft is piloted as a normal small-scale helicopter, but without the need for a tail rotor to counteract the main rotor torque.

3. Simulation model

3.1. Overview of the simulation model

The dual-rotor VTOL is modeled under the hypothesis of a rigid body moving in a flat and not-rotating Earth under the action of propulsive, aerodynamic, and gravity effects. The resulting 14 DoF model is made of 14 nonlinear equations: six for the first-order rigid body motion, six for the second-order main rotor flapping (3 for each rotor), and two for the first-order main rotor dynamic inflow. The rotor angular velocity is kept constant and the analysis will focus on flight conditions that are generally operated at constant RPM. A uniform, first-order, inflow model based on general momentum theory is employed. The structure of the mathematical model is represented by the closed-loop block diagram in Figure 2. The pilot input, together with the current state of the rotorcraft passes through a control system, whose design is out of the scope of this paper, and then split into the two main rotors. The rotor dynamics is addressed at first, with the flapping and inflow equations solved for each rotor. Finally, the rigid-body equations of motion are solved under the effect of three external forces and moments contributions, i.e. the two main rotors and the fuselage aerodynamic force.

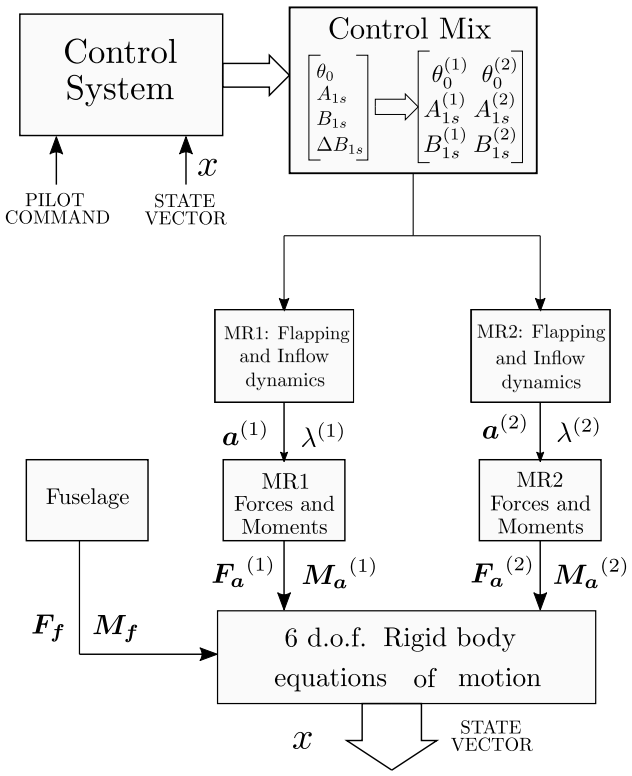

Figure 2: Scheme of the simulation model

3.2. Main rotor

The two main rotors are modeled as semi-rigid ones, according to the mathematical framework developed by Talbot [35]. The same model characterizes both rotors, with the only difference related to the hub position with respect to the rotorcraft center of mass and the sense of rotation. For the sake of simplicity, in this section, the framework is presented for a generic rotor.

The blades are assumed to be rigid and their forces and moments are integrated along the blade span and around one revolution to obtain an

analytical expression of the loads in the local hub-body frames. In particular, while the expression of these forces can be found in [35], a correction for the clockwise rotor is applied according to Choi *et al.* [36]. The correction involves the use of symmetrical, local hub-body coordinate systems for the two rotors, thus a right-handed one for the counter-clockwise rotor ($\Gamma = 1$) and a left-handed one for the clockwise rotor ($\Gamma = -1$), as depicted in Figure 3. According to this correction, the wind ad angular velocities in hub-body frames for a generic rotor can be expressed as (considering that no incidence is applied to the rotors)

$$\boldsymbol{\omega}_H = \begin{bmatrix} \Gamma & 0 & 0 \\ 0 & 1 & 0 \\ 0 & 0 & \Gamma \end{bmatrix} \boldsymbol{\omega}_B \tag{3}$$

$$\boldsymbol{U}_H = \begin{bmatrix} 1 & 0 & 0 \\ 0 & \Gamma & 0 \\ 0 & 0 & 1 \end{bmatrix} \boldsymbol{U}_B + \boldsymbol{\omega}_H \times \boldsymbol{r}_H \tag{4}$$

The lateral cyclic control input has to be corrected as well when expressed in the hub-body frame as

$$A_{1s}|_H = \Gamma A_{1s}|_B \tag{5}$$

Finally, the aerodynamic forces and moments expressed in body axes ($\boldsymbol{F}_a$

and $\boldsymbol{M}_a$) can be found as

$$\boldsymbol{F}_a = \begin{bmatrix} \cos\beta_w & \sin\beta_w & 0 \\ -\Gamma\sin\beta_w & \Gamma\cos\beta_w & 0 \\ 0 & 0 & 1 \end{bmatrix} \begin{bmatrix} -H_w \\ Y_w \\ -T_r \end{bmatrix} \tag{6}$$

$$\boldsymbol{M}_a = \begin{bmatrix} \Gamma\cos\beta_w & \Gamma\sin\beta_w & 0 \\ -\sin\beta_w & \cos\beta_w & 0 \\ 0 & 0 & \Gamma \end{bmatrix} \begin{bmatrix} L_w \\ M_w \\ Q \end{bmatrix} + \boldsymbol{r}_H \times \boldsymbol{F}_a \tag{7}$$

where the expression of the horizontal force H_w, lateral force Y_w, rotor thrust T_r, rolling moment L_w, pitching moment M_w and torque Q can be found in Talbot [35] expressed in hub-wind frame of reference. The sign conventions for the angles follow the right-handed body frame of reference reported in Figure 3: positive pitch, roll, and yaw angles are intended to as, respectively, a nose-up, MR1 down (rolling to the right) and clockwise rotations of the body.

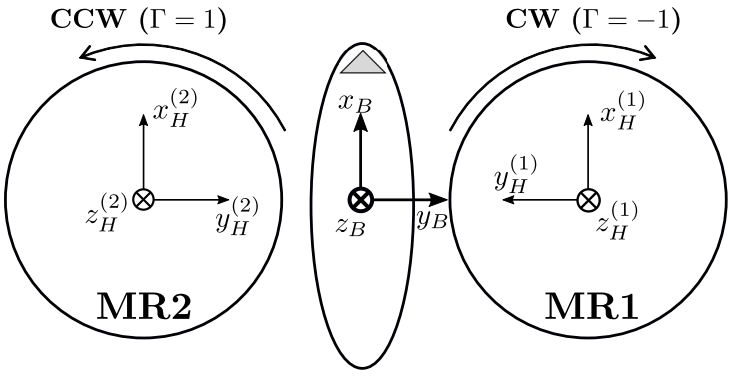

Figure 3: Rotorcraft coordinate systems.

The mathematical model of the main rotor includes a uniform, nonlinear, induced inflow ratio (λ_i) model derived from general momentum theory [37]. In particular, its dynamics can be expressed as

$$\dot{\lambda_i} = \frac{3\pi}{4}\left(\frac{C_T}{2} - \lambda_i\sqrt{\mu^2+\lambda}\right) \tag{8}$$

where the total inflow $\lambda = \lambda_i + \frac{w_H}{\Omega R}$ and the uniform, time-dependent, rotor-induced velocity is defined as $v_i = \lambda_i \Omega R$.

The blade flapping is approximated by the tip path plane (TPP) representation

$$\beta(t) = a_0(t) - a_1(t)\cos\psi_b - b_1(t)\sin(\psi_b) \tag{9}$$

where time-varying coefficients a_0, a_1, and b_1 follow the second-order dynamics law developed by Chen [38, 39]. The TPP dynamics can be expressed as

$$\ddot{\boldsymbol{a}} + \tilde{D}\dot{\boldsymbol{a}} + \tilde{K}\boldsymbol{a} = \tilde{\boldsymbol{f}} \qquad \text{where} \qquad \boldsymbol{a} = [a_0\ a_1\ b_1]^T \tag{10}$$

and matrixes $\tilde{D}$, $\tilde{K}$ and $\tilde{f}$ can be found in the reference [39]. a_0, a_1, and b_1 are respectively the coning, longitudinal, and lateral flapping coefficients.

For the sake of simplicity, a linear lift coefficient curve is adopted for the simulation at low angles of attack (α). However, a correction factor k_{C_L} is added to take into account blade stall effects and provide more realistic results when the incidence on the blade profile overcomes the maximum lift condition. For the sake of this analysis, a *NACA0015* airfoil is used, and

look-up tables [40] are employed to evaluate the average (from a Reynolds number point of view) C_{L_α} and stall lift and drag coefficient C_{D_s} and C_{L_s}. In particular, the values $C_{L_\alpha} = 4.54$, $C_{L_s} = 1.12$ and $C_{D_s} = 0.052$ are used. Figure 4 shows the lift curve in a range of α between -12° and 90°. It is noticeable that the slope remains constant until the C_L approaches its maximum value while, above this limit, the lift follows the analytical, approximate, expression proposed by Viterna [41] for post-stall regions. Being α_s the average stall angle and C_{L_α} the curve slope in the pre-stall regime,

$$C_L = k_{C_L} C_{L_\alpha} \alpha \qquad \text{where} \qquad k_{C_L} = \begin{cases} 1 & \text{if } \alpha < \alpha_s \\ \dfrac{1}{C_{L_\alpha}} \dfrac{dC_L}{d\alpha} & \text{if } \alpha > \alpha_s \end{cases} \tag{11}$$

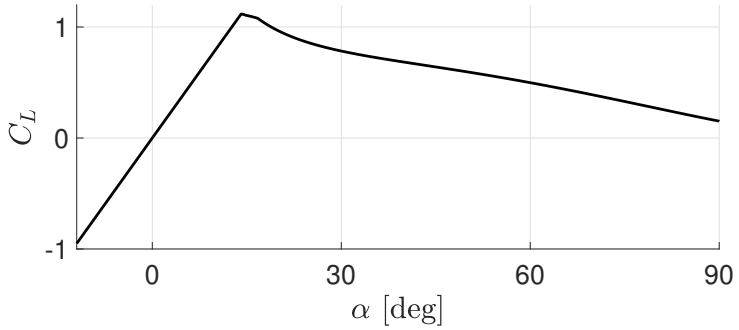

Figure 4: C_L curve NACA0015 with Viterna correction

Before implementing the side-by-side rotorcraft, the main rotor model was validated against a higher fidelity F-L-P (Flap, Lag, Pitch) numerical framework, showing good agreement in the input responses. The model, already developed and verified with commercial software for single rotor con-

figuration, was developed by Tamallah [42] and includes coupled second-order flapping and lead-lag dynamics, as well as a non-uniform inflow.

3.3. Shroud modeling

The effect of the shroud is accounted by extending momentum theory to the analysis of a ducted fan. Theoretical analysis conducted by Kruger [43] has shown that the presence of a shroud may be beneficial for rotor performance by decreasing the power required to produce the same amount of thrust. By following the approach presented by Leishman [44], the total thrust T produced by the ducted rotor can be computed as the sum of two contributions:

$$T = T_r + T_d \qquad \text{where} \qquad \frac{T_d}{T} = 1 - \frac{1}{2a_w} \, . \tag{12}$$

T_d is an additional contribution that arises from the presence of the shroud and depends on the wake contraction factor a_w generated by the geometry of the shroud itself. Accurate estimation of a_w is a challenging task from both a numerical and an experimental point of view. Different analyses can be found in the literature for improving the accuracy of fan-in-fin tail rotor models or ducted fans [45, 46]. While an extensive aerodynamic study would be required to evaluate the interaction between the rotor and the shroud, for the sake of this study an analytical and simple model is preferred. The semi-analytical mathematical model developed by Bourtsev *et al.* [47] is indeed adopted for the present case, as it directly relates the duct geometry to pressure losses evaluated by experimental tests. In particular, "lip" duct

inlet and outlet are considered, with a lip radius (r_k) of 0.01 m and a blade tip clearance (δ) of 0.01 m. The wake contraction factor is computed as

$$a_w = \frac{1}{2}\left(1 + \delta_f \left[\frac{K_v}{2} + \frac{(\xi_{in} + \xi_{out})}{2K_v} - 1\right]\right)^{-1} \tag{13}$$

ξ_{in} is evaluated as a function of the lip radius according to the experimental data provided by Bourtsev *et al.* [47], while ξ_{out} is equal to zero.

3.4. Fuselage

A bottleneck of the analysis is the estimation of the fuselage aerodynamic loads. In a preliminary analysis, the equivalent flat plat area approach is adopted to characterize fuselage aerodynamics. In this respect, a set of equivalent surfaces, each characterized by a specific parasite drag, is considered. The latter hypothesis involves the assumption that the fuselage behaves as a non-lifting body, thus the force generated while moving in the air is only a parasite drag, aiming in the direction of relative airspeed. The fuselage is approximated as depicted in Figure 5, where the three main flat plates (frontal, top, and side) are characterized by their surface and drag coefficient. The fuselage drag is computed as a sum of the contributions from the three flat plates, which depends on the orientation of the incoming flow. In particular $D = D^f + D^t + D^s$, where

$$D^f = \frac{1}{2}\rho U_\infty^2 S^f C_D^f (\hat{U} \cdot \hat{x}) \tag{14}$$

$$D^s = \frac{1}{2}\rho U_\infty^2 S^s C_D^s (\hat{U} \cdot \hat{y}) \tag{15}$$

$$D^t = \frac{1}{2}\rho U_\infty^2 S^t C_D^t (\hat{U} \cdot \hat{z}) \tag{16}$$

Superscripts ^{f}, ^{s}, and ^{t} refer to frontal, side and top areas. The scalar product between the surface normal and the velocity versor determines the portion of the flat plate invested by the flow. The values of the equivalent surfaces and relative parasite drag coefficients, reported in Table 2, are estimated by using a simplified geometry of the vehicle modeled with OpenVSP (Figure 6) [48].

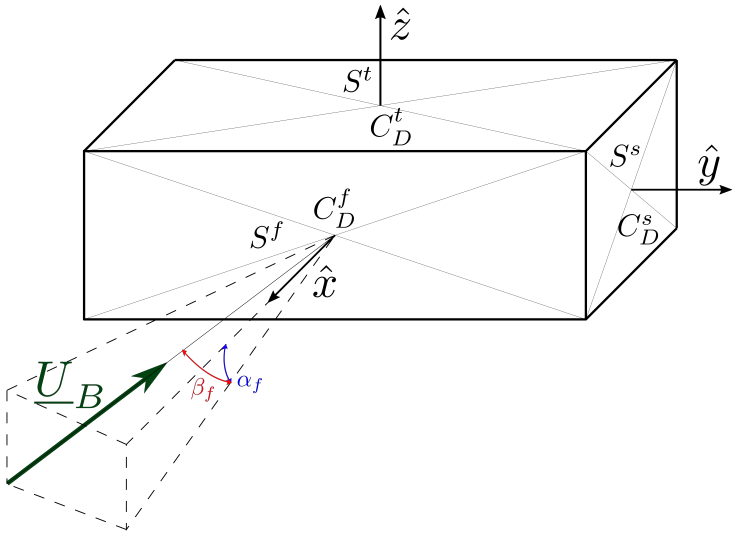

Figure 5: Flat plate approximation for the fuselage aerodynamics

$S^f = 0.3426$ m^2	$S^s = 0.2065$ m^2	$S^t = 0.8034$ m^2
$C_D^f = 0.3854$	$C_D^s = 0.6356$	$C_D^t = 0.1645$

Table 2: Reference surfaces and drag coefficients of the equivalent flat plate fuselage approximation

Estimating the center of pressure (CP) is another important aspect of fuselage modeling. Still, a complete aerodynamic analysis would be needed, but

for the sake of this paper and according to the symmetry planes that characterize the vehicle, it is assumed that the aerodynamic force can be applied in front of the CG, along the longitudinal plane. In this way, the fuselage will only contribute with pitching and yawing moments, respectively when different angles of attack and sideslip occur. In particular, the CP is assumed to be placed at 1/3 of the parallelepiped depth, thus 0.26 m in front of the CG. The latter is a general approximation that is made by recalling flat-plates aerodynamic theory [40] and by comparing with fuselage aerodynamic results of similar configurations [49, 50]. The forces and moments in body axes can be expressed as

$$\boldsymbol{F}_f = -D\hat{\boldsymbol{U}} \qquad \text{and} \qquad \boldsymbol{M}_f = \boldsymbol{r}_{CP} \times \boldsymbol{F}_f \tag{17}$$

where $\boldsymbol{r}_{CP}$ is the position vector of the center of pressure.

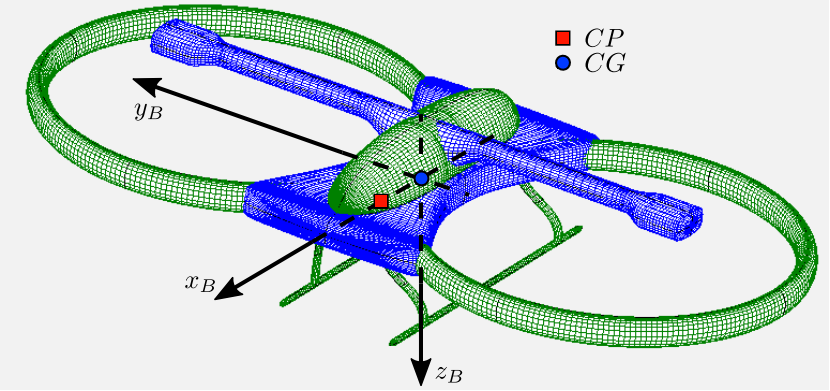

Figure 6: Fuselage modeling in OpenVSP

4. Trim routine

An iterative algorithm based on the Newton-Raphson method is implemented to compute the trim conditions of the vehicle at different velocities. A system of 14 unknowns and 14 equations is solved. The input of the system are the velocity in the inertial frame and the angular velocities in the body frame $\boldsymbol{\omega}_B$. The rotor angular rates are kept constant to their nominal values and a zero yaw angle is imposed. The system of equations to be solved is the following:

$$\begin{cases} \left[\tilde{K}\boldsymbol{a} - \tilde{\boldsymbol{f}}\right]^{(1)} = 0 \\ \left[\tilde{K}\boldsymbol{a} - \tilde{\boldsymbol{f}}\right]^{(2)} = 0 \\ \boldsymbol{F}_a^{(1)} + \boldsymbol{F}_a^{(2)} + \boldsymbol{F}_g + \boldsymbol{F}_i + \boldsymbol{F}_f = 0 \\ \boldsymbol{M}_a^{(1)} + \boldsymbol{M}_a^{(2)} + \boldsymbol{M}_i + \boldsymbol{M}_f = 0 \\ A_{1s}^{(1)} = A_{1s}^{(2)} \\ \theta_0^{(1)} = \theta_0^{(2)} \end{cases} \tag{18}$$

and the vector of unknowns is

$$\left[a_0^{(1)}\ a_1^{(1)}\ b_1^{(1)}\ a_0^{(2)}\ a_1^{(2)}\ b_1^{(2)}\ \theta_0^{(1)}\ A_{1s}^{(1)}\ B_{1s}^{(1)}\ \theta_0^{(2)}\ A_{1s}^{(2)}\ B_{1s}^{(2)}\ \theta\ \phi\right]^T \tag{19}$$

where θ and ϕ are the attitude pitch and roll angles. The same modeling approach described in Section 3 is applied to both of the rotors. The first six equations are obtained imposing steady conditions to the flapping dynamics (Equation 10), namely $\dot{\boldsymbol{a}} = \ddot{\boldsymbol{a}} = 0$. The second six are the total force and moment acting on the rotorcraft. In particular, while $\boldsymbol{F}_a$, $\boldsymbol{M}_a$, $\boldsymbol{F}_f$ and $\boldsymbol{M}_f$

have already been presented in sections 3.2 and 3.4, the gravitational force $\boldsymbol{F}_g$ and inertial force and moment, $\boldsymbol{F}_i$ and $\boldsymbol{M}_i$ can be computed as

$$\boldsymbol{F}_g = m_{to} \begin{bmatrix} -g \sin\theta \\ g \sin\phi \cos\theta \\ g \cos\phi \cos\theta \end{bmatrix} \tag{20}$$

$$\boldsymbol{F}_i = -(\boldsymbol{\omega}_B \times \boldsymbol{U}_B) m_{to} \tag{21}$$

$$\boldsymbol{M}_i = -\boldsymbol{\omega}_B \times I\boldsymbol{\omega}_B \tag{22}$$

The yaw angle ψ is equal to zero. The last two equations are additional relations that are added to close the system: a constraint on the control mix is set, such that the two rotors operate at the same collective pitch and lateral cyclic, both commanded by the pilot input (see Section 2). Figures 7 and 8 report the results for different forward and lateral speeds.

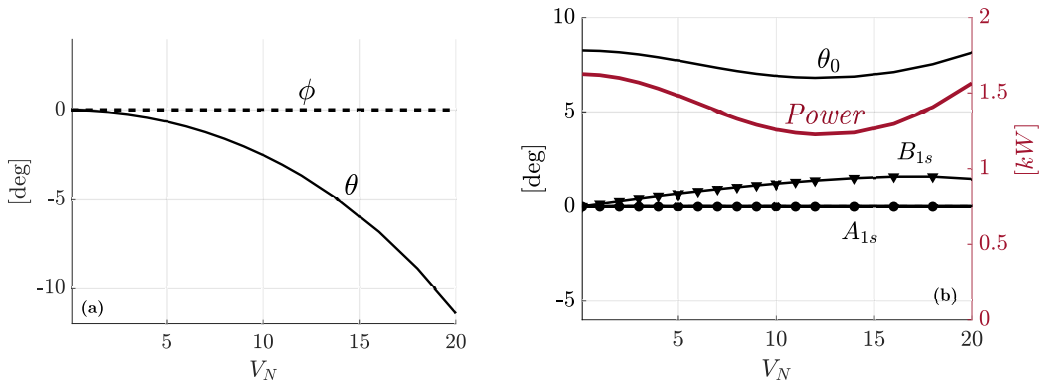

Figure 7: Trim conditions at variable forward speed: rotorcraft attitude (a) and control inputs (b)

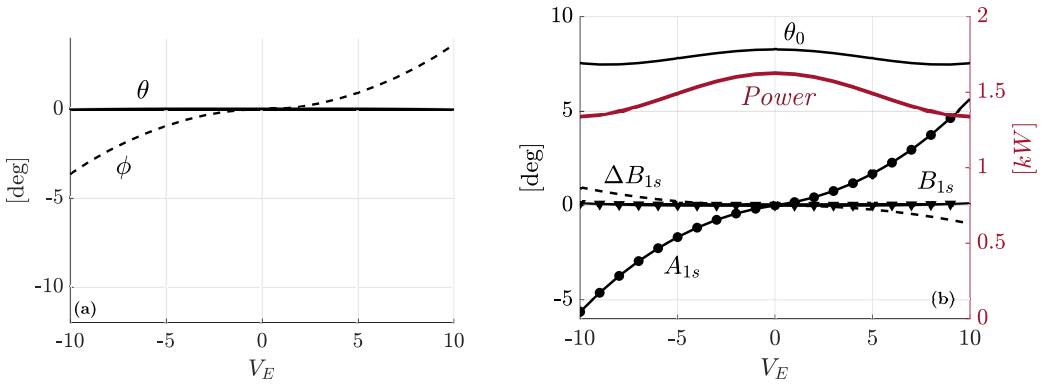

Figure 8: Trim conditions at variable lateral speed: rotorcraft attitude (a) and control inputs (b)

Figure 7 (a) reports the attitude of the rotorcraft as a function of the forward speed. The aircraft pitches down as the speed increases, while a positive longitudinal cyclic B_{1s} is applied (Figure 7 (b)). It is noted that, according to the mathematical model presented in Section 3.2, a positive longitudinal cyclic is intended to be a "push effort" by the pilot, while the attitude signs are defined by the right-handed body axes system. The roll angle ϕ of the rotorcraft remains close to zero as well as the lateral cyclic effort. Together with the B_{1s}, the collective pitch changes by following the trend of the power. The aircraft absorbs around 1.6 kW at hover and has a minimum power of 1.2 kW, obtained at 12 m/s. As the speed increases, the pitching moment generated by the fuselage becomes stronger due to the higher negative θ and the CP position in front of the CG. The latter produces a decrease of the B_{1s} curve slope, nearly reducing the pilot's effort to maintain the steady condition.

In order to perform a lateral motion, the aircraft rolls in the direction of the speed (ϕ angle in Figure 8 (a)) by following the pilot's lateral cyclic input reported in Figure 8 (b). Together with the A_{1s} control, which is positive in the positive direction of the lateral speed, and the collective pitch, which still follows the power trend, a small contribution of the differential longitudinal cyclic should be introduced to counteract the yawing moment induced by the fuselage. Indeed, the $\boldsymbol{r}_{CP}$ position in front of the CG generates an unstable moment about the z-axis when the rotorcraft is subjected to a sideslip angle.

5. Linearization of the dynamic model

In order to study the open-loop stability of the dual-rotor configuration, a linear model about a trim condition is developed. The 6 d.o.f. rigid body equations of motion in vector form can be written as follows:

$$\begin{cases} m_{to}\dot{\boldsymbol{U}}_{\boldsymbol{B}} & = -m_{to}\boldsymbol{\omega}_{\boldsymbol{B}} \times \boldsymbol{U}_{\boldsymbol{B}} + \boldsymbol{F}_{\boldsymbol{g}} + \boldsymbol{F} \\ I\dot{\boldsymbol{\omega}}_{\boldsymbol{B}} & = \boldsymbol{Mom} - \boldsymbol{\omega}_{\boldsymbol{B}} \times I\boldsymbol{\omega}_{\boldsymbol{B}} \end{cases} \tag{23}$$

where the excitation of this first-order system is represented by the sum of the external forces ($\boldsymbol{F} = [XYZ]$) and moments ($\boldsymbol{M} = [LMN]$) acting on the rotorcraft. Note that the external force and moment include in their definition the aerodynamic forces/moments of the two rotors ($\boldsymbol{F}_{\boldsymbol{a}}^{(\mathbf{1})}$ and $\boldsymbol{F}_{\boldsymbol{a}}^{(\mathbf{2})}$) and the fuselage ($\boldsymbol{F}_{\boldsymbol{f}}$). Considering the state vector $x = [u\ w\ q\ \theta\ v\ p\ \phi\ r]$ and control vector $\tau = [\theta_0\ A_{1s}\ B_{1s}\ \Delta B_{1s}]$, the system can be linearized by applying small perturbation theory a by neglecting second order and smaller

terms [51]. Note that the heading angle ψ is neglected as it does not affect the dynamics of the rotorcraft. In particular, each state is described as a perturbation from the trim condition, thus $x = x^0 + \delta x$, where superscript ^{0} identifies the trim condition and δx is a small perturbation. The excitation is linearized by employing a Fourier series such that a general force/moment can be expressed as its trim value (F^0) plus a sum of contributions from each state and control variable, such that

$$\boldsymbol{F} = \boldsymbol{F^0} + \boldsymbol{F}_u u + \boldsymbol{F}_w w + ... + \boldsymbol{F}_{\Delta B_{1s}} \Delta B_{1s} \tag{24}$$

where the first-order derivative about a generic perturbation δx_i of the x_i state is computed numerically with a central finite difference formula as

$$\boldsymbol{F}_{x_i} = \frac{\partial \boldsymbol{F}}{\partial x_i}\Big|_{x_i^0} = \frac{\boldsymbol{F}(x_i^0 + \delta x_i) - \boldsymbol{F}(x_i^0 - \delta x_i)}{2\delta x_i} \tag{25}$$

and are called "stability derivatives". The value of the perturbation is chosen by performing a convergence check on the derivatives to not affect their computation. In particular, 10% of the forward velocity is chosen for the forward speed perturbation, 0.1 m/s is used for the other two components while a perturbation of 0.01 rad/s is applied to the angular velocities and 0.1 degrees for the attitude and control angles.

Finally, the linearized 6 d.o.f. equations of motion, around a trim condi-

tion with no angular rates ($p^0 = q^0 = r^0 = 0$) are described by the system

$$\begin{cases} \dot{u} &= -w^0 q - g\theta\cos\theta^0 + v^0 r + X_u u + X_w w + ... + X_{\Delta B_{1s}}\Delta B_{1s} \\ \dot{w} &= u^0 q - g\theta\cos\phi^0\sin\theta^0 - v^0 p - g\phi\sin\phi^0\cos\theta^0 + Z_u u + Z_w w + ... + Z_{\Delta B_{1s}}\Delta B_{1s} \\ \dot{q} &= M_u u + M_w w + ... + M_{\Delta B_{1s}}\Delta B_{1s} \\ \dot{\theta} &= q\cos\theta^0 - r\sin\theta^0 \\ \dot{v} &= -g\theta\sin\phi^0\sin\theta^0 + pw^0 - ru^0 + Y_u u + Y_w w + ... + Y_{\Delta B_{1s}}\Delta B_{1s} \\ \dot{p} &= L'_u u + L'_w w + ... + L'_{\Delta B_{1s}}\Delta B_{1s} \\ \dot{\phi} &= p + q\sin\phi^0\tan\theta^0 + r\cos\phi^0\tan\theta^0 \\ \dot{r} &= N'_u u + N'_w w + ... + N'_{\Delta B_{1s}}\Delta B_{1s} \end{cases} \tag{26}$$

which in matrix form can be written as $\dot{x} = Ax + B\tau$, where x and τ are the motion state and control perturbation vectors, while A and B are the system's state and control matrices [51]. The force derivatives (X, Y, and Z) are normalized with m_{to}, while the pitching moment (M) are normalized with the inertia moment with respect to the pitch axis I_{yy}. The lateral-directional derivatives L' and N' are normalized and coupled as

$$L'_{x_i} = \frac{I_{zz}L_{x_i} + I_{xz}N_{x_i}}{I_c} \tag{27}$$

$$N'_{x_i} = \frac{I_{xz}L_{x_i} + I_{xx}N_{x_i}}{I_c} \tag{28}$$

where $I_c = I_{xx}I_{zz} - I_{xz}^2$.

The dynamic stability of the system can be assessed by considering the eigenvalues of the state matrix A. Figure 9 reports the set of eigenvectors related to each pole of the system. The poles are identified by an ID and reported above each plot. According to the eigenvectors analysis, a first classification can be performed between the modes governing the longitudinal and lateral-directional dynamics. Four longitudinal modes with similar frequency can be identified, where two complex conjugate poles represent an oscillating motion governed by the forward speed u and a complex, small, pitch and heave contribution. These two oscillatory modes can be most likely related to stable phugoid or heave subsidence dynamics. A couple of stable/unstable real poles characterized by u and w contributions are also present, most likely representing heave subsidence or short-period dynamics. Indeed, it is still unclear whether these longitudinal poles reproduce the classical modes of conventional aircraft but an extensive analysis will be performed in the next chapter. From the lateral-directional point of view, four real poles are present. A higher-frequency stable one is governed by lateral speed and a small contribution of roll rate and angle, while a very low-frequency, slightly stable, lateral mode can be identified in a yaw subsidence behavior governed by the yaw rate r and lateral speed v.

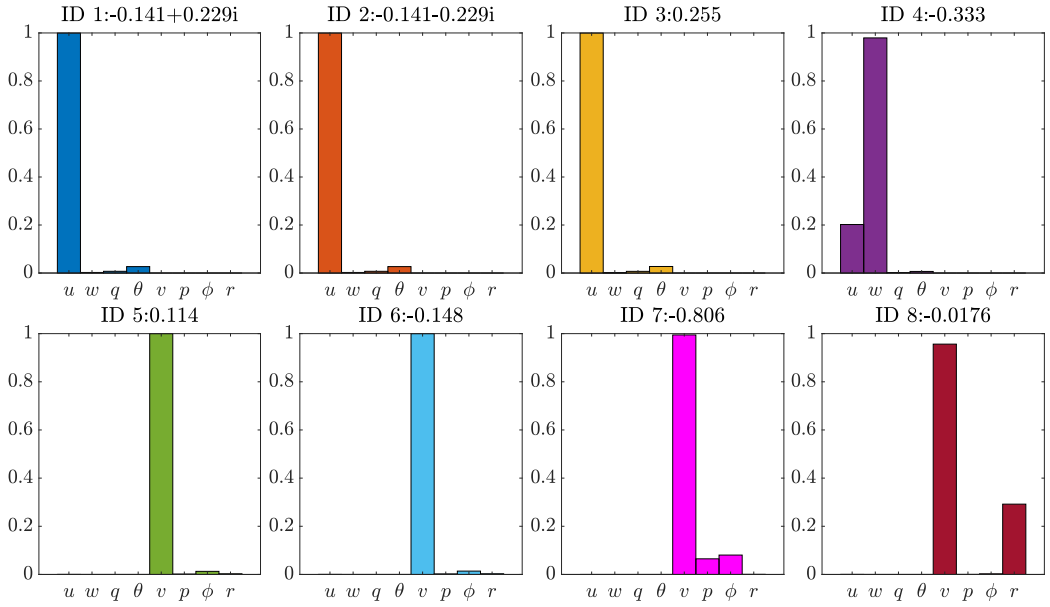

Figure 9: Eigenvectors representation in hovering condition

6. Results

6.1. Variable forward speed dynamics

The linearized model described in Section 5 is used to study the stability of the system in each of its characteristic modes and with an increasing forward speed. Figure 13 shows the evolution of the system's poles in a complex plane, while Figure 10 reports their natural frequency in a semi-logarithmic plot. In addition, Figure 14 plots the participation of the 8 modes in each of the rotorcraft poles while Figure 11 shows the stability of the different dynamics by plotting their real part. From the latter, it can be observed that the increase in forward speed worsens some of the instabilities already present in hovering, however, it does not give rise to new ones. The static stability of the system is reported in Figure 12, with the evolution of

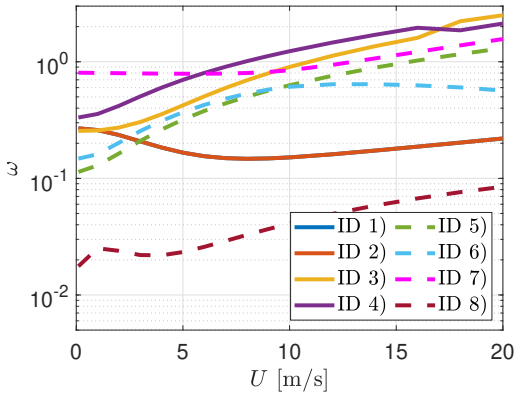

Figure 10: Logarithmic plot of the poles' frequency at variable forward speed

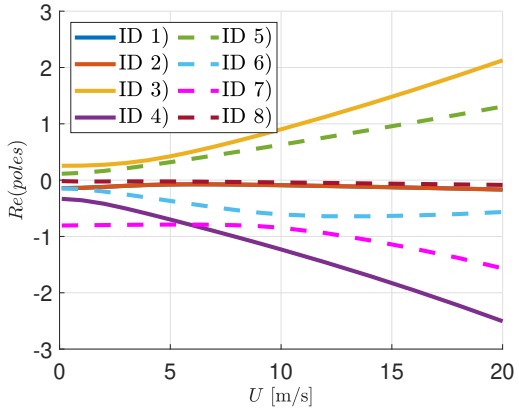

Figure 11: Real part of the system's poles at variable forward speed

the derivative M_w: the rotorcraft is statically unstable and this condition is worsened by the increase of forward speed. The longitudinal dynamic of the system, i.e. *ID 1*, *ID 2*, *ID 3*, and *ID 4*, is characterized by a couple of complex conjugates and two real poles. *ID 1* and *ID 2* represent low-frequency, oscillatory, dynamics governed by the forward velocity u and a complex contribution of the vertical speed w. The behavior of these poles may be associated with a stable aircraft phugoid/heave subsidence mode. On

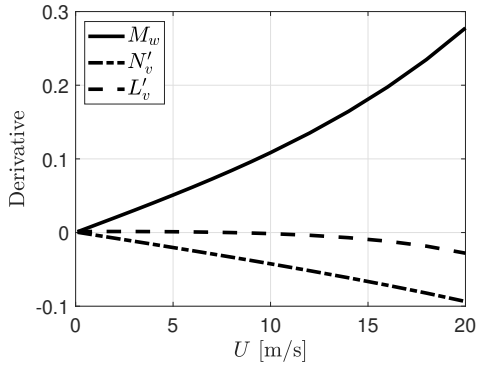

Figure 12: Evolution of the static stability M_w and sideslip derivatives N'_v (weathercock stability) and L'_v (dihedral effect) for a variable forward speed.

the other hand, *ID 3* and *ID 4* seem most likely to be related to short-period dynamics, being characterized by a higher frequency and the participation of the pitch angle and pitch rate (Figure 14) that arises as the forward speed increases. The positive one provides a strong longitudinal instability.

By looking at the lateral-directional dynamics, i.e. *ID 5*, *ID 6*, *ID 7*, and*ID 8*, a very low frequency, slightly unstable, the real pole is present (*ID 8)*, representing what is most likely traceable to a spiral mode. The latter is indeed characterized by either the yaw rate and roll angle, together with the forward/lateral speed. *ID 5*, *6* and *7* are instead three real poles that develop with similar frequencies and are characterized by the main contribution of the lateral speed, together with yaw and roll rates that grow and decrease according to the velocity regime. Another important aspect of the directional dynamics is related to the weathercock instability that arises with a negative N'_v (Figure 12). As a matter of fact, the CP position in front of the CG and the absence of a vertical fin to dampen the yaw rate, make the system

directionally unstable.

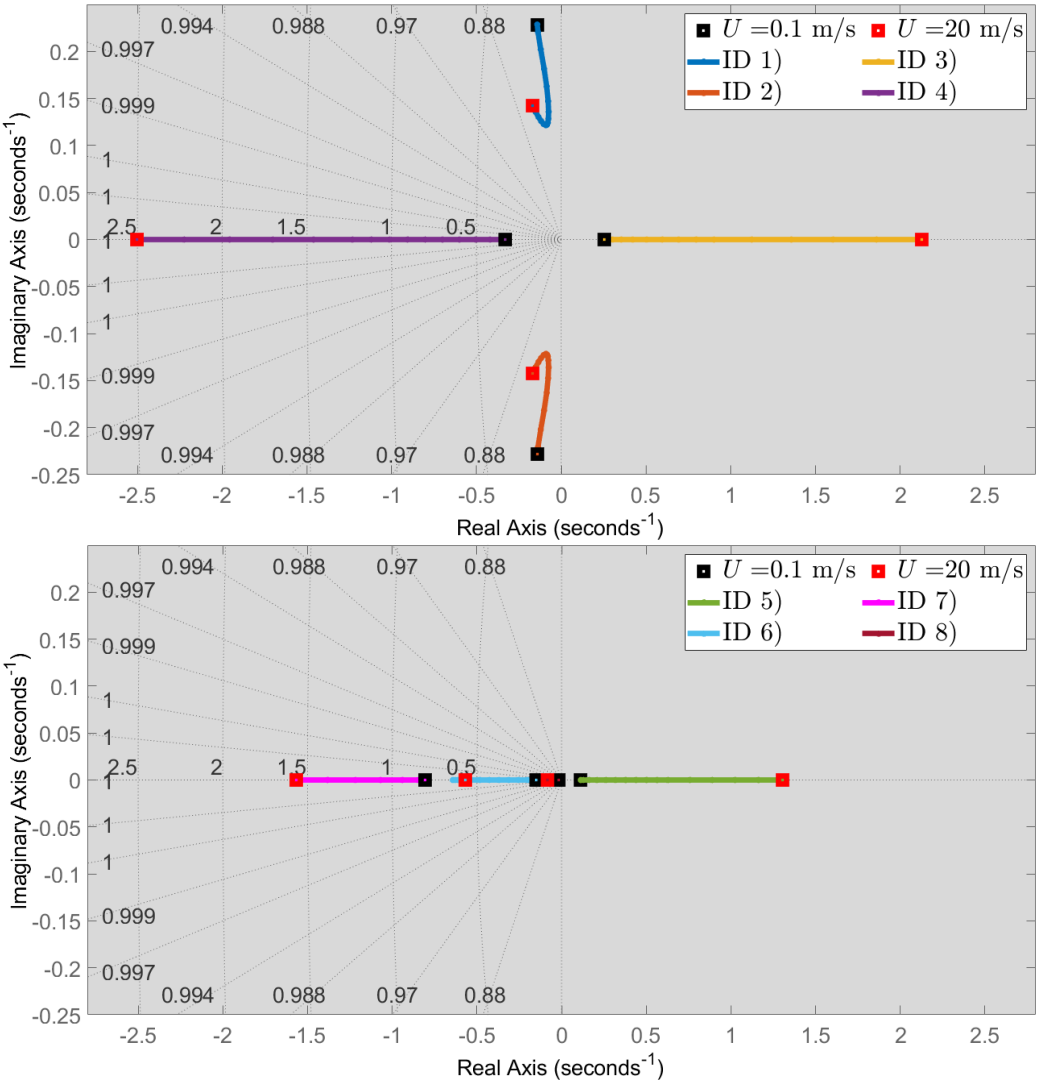

Figure 13: Evolution of the longitudinal (above) and lateral (below) poles at variable forward speed. The black/red squares indicate the initial (hovering) and final (U = 20 m/s) point

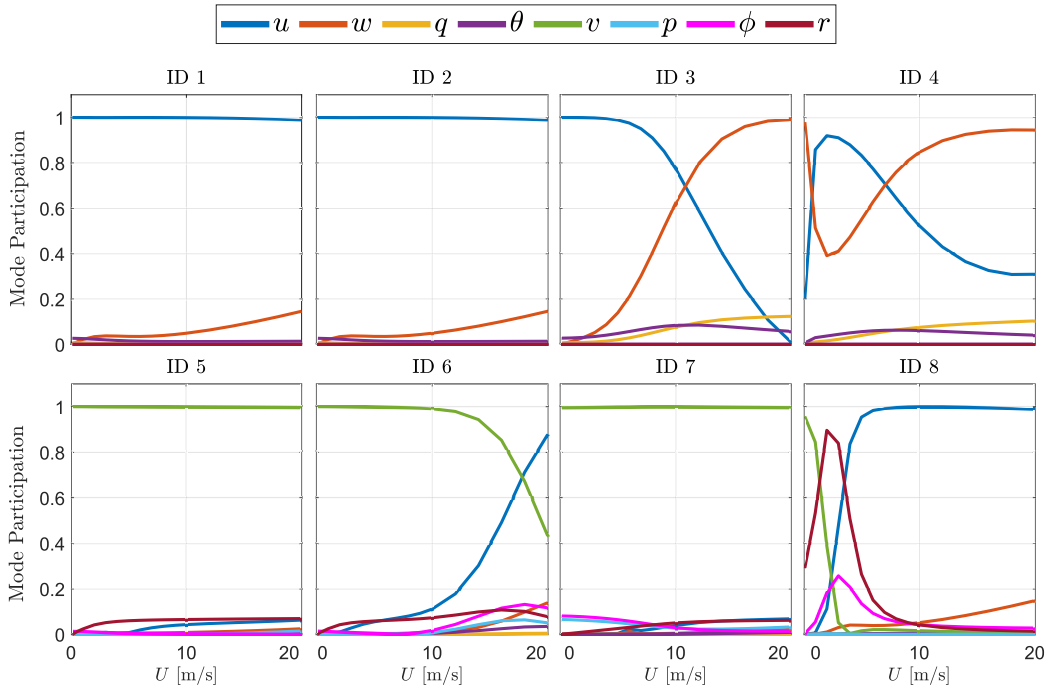

Figure 14: Plot of the participation of each mode for each eigenvalue

6.2. Variable center of gravity dynamics

In order to account for eVTOL applications, where the batteries are located and can be shifted along the longitudinal axis, this section elaborates on the effect of the CG on vehicle stability. The analysis presented in Section 6.1 describes the stability of the system with a CG placed on the symmetry plane of the vehicle, which is also aligned with the application of the main rotor force. In the present Section, the CG is shifted along the x-axis of a ΔCG, and the stability is studied. A schematic view of the rotorcraft is reported in Figure 15 to highlight the relative position of these points. Figure 17 reports the evolution of the longitudinal and lateral poles of the system at $U = 10$ m/s and within an interval of $\Delta CG = \pm 0.2$ m. Figures 18 and 19

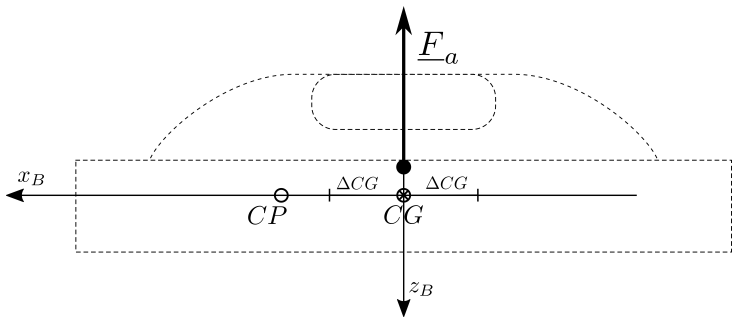

Figure 15: Schematic side representation of the rotorcraft's CG, CP, and main rotor force application.

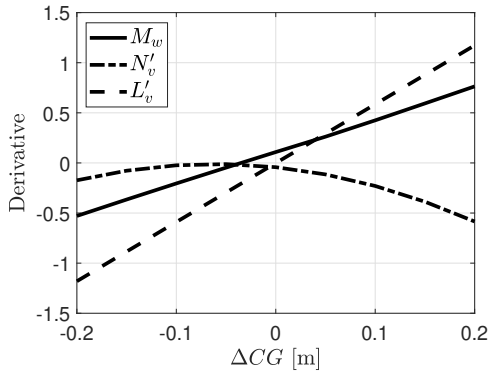

Figure 16: Evolution of the static stability M_w and the sideslip derivatives N'_v (weathercock stability) and L'_v (dihedral effect) for a variable ΔCG at $U = 10$ m/s.

report the eigenvectors of the system for two opposite CG positions.

It can be observed that the two longitudinal low-frequency poles (*ID 1* and *ID 2*), identified as a phugoid/heave subsidence mode in the previous section, become real as soon as the CG is shifted along the x-axis and misaligned with the rotor's arms. Therefore, it can be assumed that the oscillating low-frequency behavior was associated with the vertical alignment between the rotors and the CG. On the other hand, the two poles representing the high-frequency longitudinal dynamics *ID 3* and *ID 4*, associated with

a pitch and heave behavior, become negative and oscillatory when the CG is shifted backward, making the system's short period stable.

Concerning lateral stability, as soon as $\Delta CG \neq 0$, lateral phugoid (also known as dutch-roll in general aircraft nomenclature), roll, and spiral dynamics can be identified. Indeed, a couple of complex conjugate poles, characterized by lateral speed, roll, and yaw rates can be most likely traceable to a lateral phugoid mode, while the high-frequency real pole represents the roll one. In particular, placing the CG behind the rotors ($\Delta CG < 0$) can be beneficial for the roll dynamics but drives the oscillatory poles towards the positive plane. This can be linked to the evolution of the sideslip derivatives reported in Figure 16, which mainly affect the lateral-directional stability. Indeed, an unstable behavior is connected to negative weathercock stability and a positive dihedral effect, both of them occurring when $\Delta CG < 0$. However, this condition can be improved by installing a properly sized vertical fin, which would increase the directional stability of the system. In this way, the instability of the lateral phugoid can be limited, while the high-frequency longitudinal poles can be stabilized by moving the CG behind the rotor's arms. In addition, moving back the CG is also beneficial for the static stability of the rotorcraft, reported in Figure 16 by means of the M_w derivative. The latter becomes negative, thus stable, for negative ΔCG.

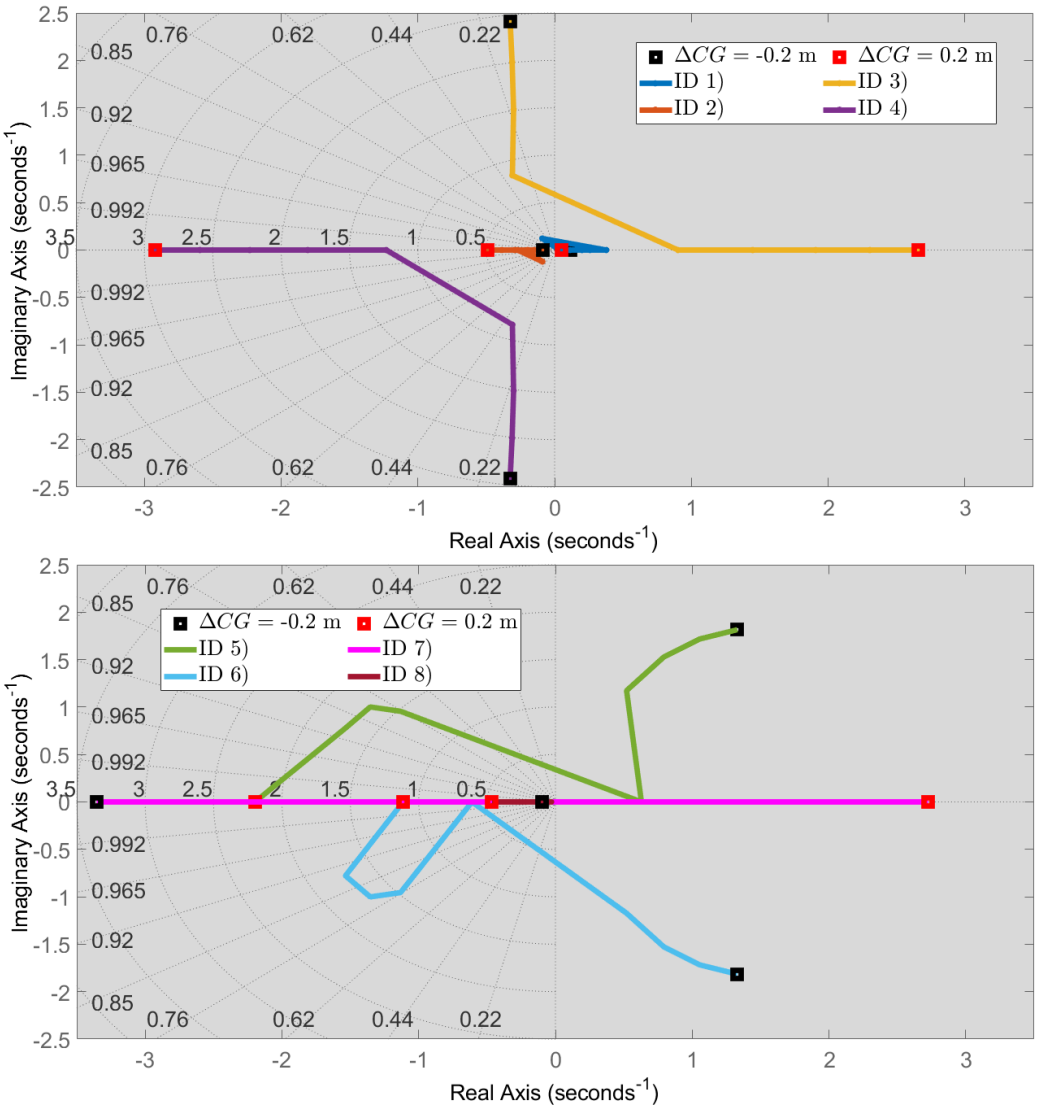

Figure 17: Evolution of the longitudinal (above) and lateral (below) poles at $U = 10$ m/s and variable CG position. The black/red squares indicate the initial ($\Delta CG = -0.2$ m) and final ($\Delta CG = 0.2$ m) locations.

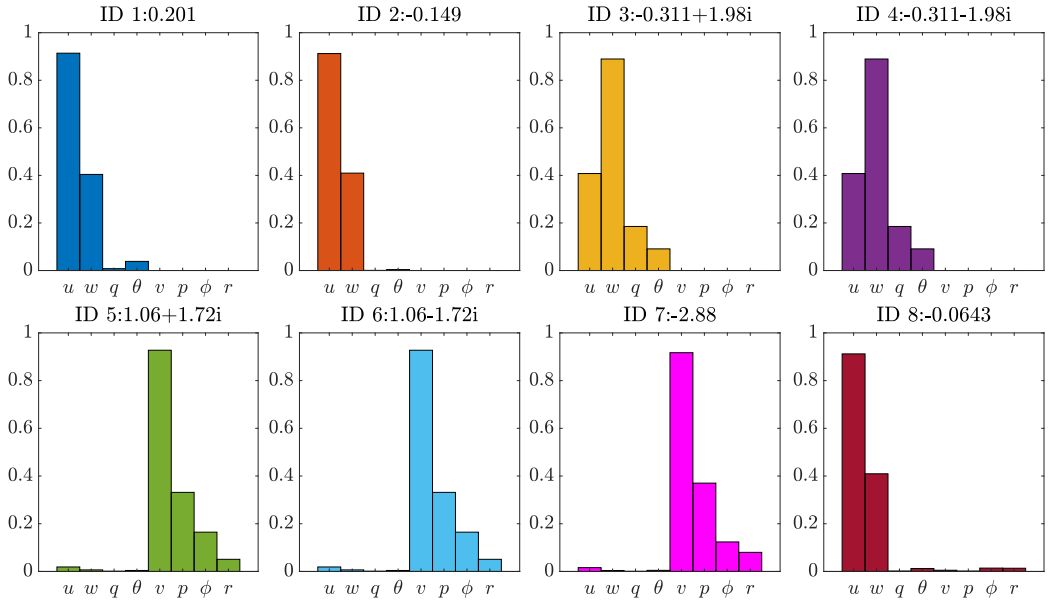

Figure 18: Eigenvectors representation at $U = 10$ m/s and $\Delta CG = -0.15$ m

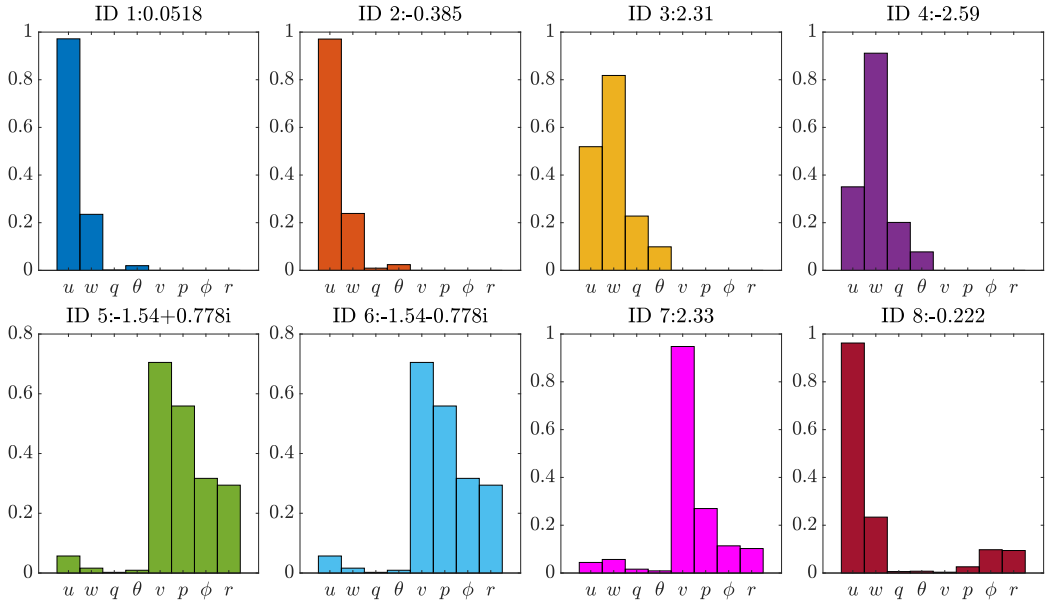

Figure 19: Eigenvectors representation at $U = 10$ m/s and $\Delta CG = 0.15$ m

7. Conclusions

The analysis presented in this paper has the aim of studying the flight dynamic properties of a small-scale electric dual rotor VTOL for urban air mobility. The configuration proposed in the paper is a side-by-side helicopter, with two identical, shrouded, and counter-rotating rotors that operate at constant angular speed. A nonlinear mathematical model is implemented and improved by considering the effect of the shrouds around the two main rotors and the fuselage aerodynamic loads.

The trim conditions of the VTOL are evaluated by solving the nonlinear system in steady state conditions: the rotorcraft reaches an equilibrium point for variable forward and lateral speed by employing reasonable ranges of controls and attitude. The rotorcraft absorbs 1.6 kW of power to keep the hovering at ground level and applies 8 deg of collective pitch in both of the rotors. A positive longitudinal cyclic, corresponding to a negative pitch angle, is applied to move forward while the lateral cyclic input is used to move laterally and impose a roll angle.

The mathematical model is linearized around the above-mentioned trim conditions and a study on the stability characteristics at different speed and CG positions is performed. In particular, an unstable high-frequency short-period mode, governed by the vertical velocity and pitch angle arises when the CG is aligned, or placed in front of the two main rotor's arms. An increase in the forward speed is detrimental for the latter dynamic. From a lateral–directional stability point of view, a stable spiral mode is present for

all of the analyzed cases, while the stability of the roll and lateral phugoid poles mainly depends on the center of gravity location. In general, unstable high-frequency roll dynamics arise as soon as the CG is placed in front of the symmetry plane, while the oscillatory poles follow an opposite trend.

In conclusion, the analyzed side-by-side helicopter configuration has the potential to become a good candidate to provide services in a UAM ecosystem, because of its simple design and societal acceptance. However, the particular case studied in the paper presents some criticalities that need to be solved. In particular, the position of the CG has to be revised and possibly moved backward, in order to avoid high-frequency instabilities (short period and roll dynamics) in the natural behavior of the rotorcraft and make the system statically stable. An unstable low-frequency phugoid mode has to be accepted since it arises as soon as the CG is misaligned with the rotor centers. In addition, the lateral phugoid mode follows an opposite trend with respect to the high-frequency poles. Further, the rotorcraft has almost no directional stability, and the position of the fuselage center of pressure in front of the CG causes a criticality in the yawing motion. A suitable sizing of a vertical fin can be performed in order to improve the directional damping of the system. An offline analysis was first performed in this paper before starting a flying campaign which would provide important information about the optimal battery location and handling qualities. The design of an attitude and velocity control system will follow with the experiments in order to stabilize the rotorcraft and improve maneuverability.

Acknowledgments: The authors acknowledge and thank SAB Group S.r.l. for providing the investigated rotorcraft prototype and sharing relevant data.

Statement of Interest: This study was carried out within the MOST - Sustainable Mobility National Research Center and received funding from the European Union Next-GenerationEU (PIANO NAZIONALE DI RIPRESA E RESILIENZA (PNRR) - MISSIONE 4 COMPONENTE 2, INVESTIMENTO 1.4 - D.D. 1033 17/06/2022, CN00000023). This manuscript reflects only the authors' views and opinions, neither the European Union nor the European Commission can be considered responsible for them.

Author contributions: Conceptualization, F.M., M.D.P., F.G., E.L.d.A.; methodology, F.M., M.D.P.,; software, F.M., D.F., G.B.; validation, F.M., G.B.; formal analysis, F.M.; investigation, F.M.; resources, F.G., E.L.d.A.; data curation, F.M.; writing—original draft preparation, F.M. and M.D.P. ; writing—review and editing, M.D.P.,D.F., G.B.,F.G., E.L.d.A.; visualization, F.M.; supervision, M.D.P., F.G., E.L.d.A..

References

[1] CO2 Emissions in 2022 – Analysis (2023).
URL `https://www.iea.org/reports/co2-emissions-in-2022`

[2] H. Ritchie, M. Roser, P. Rosado, CO and Greenhouse Gas Emissions

(2020).
URL https://ourworldindata.org/emissions-by-sector

[3] R. Goyal, C. Reiche, C. Fernando, J. Serrao, S. Kimmel, A. Cohen, S. Shaheen, Urban Air Mobility (UAM) Market Study, Tech. rep., NTRS Research Center: Headquarters (HQ), Document ID: 20190001472 (2018).
URL https://ntrs.nasa.gov/citations/20190001472

[4] R. Rothfeld, M. Fu, M. Balać, C. Antoniou, Potential Urban Air Mobility Travel Time Savings: An Exploratory Analysis of Munich, Paris, and San Francisco, Sustainability 13 (4) (2021) 2217. doi:10.3390/su13042217.

[5] R. Rothfeld, A. Straubinger, M. Fu, C. Al Haddad, C. Antoniou, Chapter 13 - Urban air mobility, in: Demand for Emerging Transportation Systems, 2020, pp. 267–284. doi:https://doi.org/10.1016/B978-0-12-815018-4.00013-9.

[6] C. Al Haddad, E. Chaniotakis, A. Straubinger, K. Plötner, C. Antoniou, Factors affecting the adoption and use of urban air mobility, Transp. Res. Part. A Policy Pract. 132 (2020) 696–712. doi:10.1016/j.tra.2019.12.020.

[7] C. Silva, W. R. Johnson, E. Solis, M. D. Patterson, K. R. Antcliff, VTOL Urban Air Mobility Concept Vehicles for Technology Development, in:

2018 Aviation Technology, Integration, and Operations Conference.
URL https://arc.aiaa.org/doi/abs/10.2514/6.2018-3847

[8] W. Johnson, C. Silva, E. Solis, Concept Vehicles for VTOL Air Taxi Operations, Tech. rep., NTRS Research Center: Ames Research Center (ARC), Document ID: 20180003381 (2018).
URL https://ntrs.nasa.gov/citations/20180003381

[9] Z. J. Chen, K. A. Stol, P. J. Richards, Preliminary design of multirotor UAVs with tilted-rotors for improved disturbance rejection capability, Aerosp. Sci. Technol. 92 (2019) 635–643. doi:10.1016/j.ast.2019.06.038.

[10] H. D. Yoo, S. M. Chankov, Drone-delivery Using Autonomous Mobility: An Innovative Approach to Future Last-mile Delivery Problems, in: 2018 IEEE International Conference on Industrial Engineering and Engineering Management (IEEM), 2018, pp. 1216–1220. doi:10.1109/IEEM.2018.8607829.

[11] M. D. Pavel, Understanding the control characteristics of electric vertical take-off and landing (eVTOL) aircraft for urban air mobility, Aerosp. Sci. Technol. 125 (2022) 107143. doi:10.1016/j.ast.2021.107143.

[12] S. Yanguo, W. Huanjin, Design of Flight Control System for a Small Unmanned Tilt Rotor Aircraft, Chinese J. Aeronaut. 22 (3) (2009) 250–256. doi:10.1016/S1000-9361(08)60095-3.

[13] X. Wang, L. Cai, Mathematical modeling and control of a tilt-rotor aircraft, Aerosp. Sci. Technol. 47 (2015) 473–492. doi:10.1016/j.ast.2015.10.012.

[14] W. Su, S. Qu, G. Zhu, S. S.-M. Swei, M. Hashimoto, T. Zeng, Modeling and control of a class of urban air mobility tiltrotor aircraft, Aerosp. Sci. Technol. 124 (2022) 107561. doi:10.1016/j.ast.2022.107561.

[15] J. F. Tan, T. Y. Zhou, Y. M. Sun, G. N. Barakos, Numerical investigation of the aerodynamic interaction between a tiltrotor and a tandem rotor during shipboard operations, Aerosp. Sci. Technol. 87 (2019) 62–72. doi:10.1016/j.ast.2019.02.005.

[16] A. Bacchini, E. Cestino, B. Van Magill, D. Verstraete, Impact of lift propeller drag on the performance of eVTOL lift+cruise aircraft, Aerosp. Sci. Technol. 109 (2021) 106429. doi:10.1016/j.ast.2020.106429.

[17] W. Johnson, C. Silva, Observations from Exploration of VTOL Urban Air Mobility Designs, Tech. rep., nTRS Research Center: Ames Research Center (ARC), Document ID: 20180007847 (2018).
URL `https://ntrs.nasa.gov/citations/20180007847`

[18] M. Ishitobi, M. Nishi, K. Nakasaki, Nonlinear adaptive model following control for a 3-DOF tandem-rotor model helicopter, Control. Eng. Pract. 18 (8) (2010) 936–943.

[19] J. M. A. Peña, S. A. R. Paredes, J. S. V. Martínez, Y. Aguilar-Molina, A Laboratory Prototype Tandem Helicopter With Two Degrees of Freedom, IEEE Access 9 (2021) 39618–39625. doi:10.1109/ACCESS.2021.3064568.

[20] J. L. Williams, Directional Stability Characteristics of Two Types of Tandem Helicopter Fuselage Models, 1954, NTRS Research Center: Ames Research Center (ARC), Document ID: 19930083960.
URL https://ntrs.nasa.gov/citations/19930083960

[21] Y. Cao, G. Li, Q. Yang, Studies of trims, stability, controllability, and some flying qualities of a tandem rotor helicopter, J. Aerosp. Eng. 223 (2) (2009) 171–177. doi:10.1243/09544100JAERO462.

[22] R. F. Stengel, J. R. Broussard, P. W. Berry, Digital flight control design for a tandem-rotor helicopter, Automatica 14 (4) (1978) 301–312. doi:10.1016/0005-1098(78)90030-4.

[23] A. Dzul, T. Hamel, R. Lozano, NONLINEAR CONTROL FOR A TANDEM ROTOR HELICOPTER, IFAC Proceedings Volumes 35 (1) (2002) 229–234. doi:10.3182/20020721-6-ES-1901.01263.

[24] S. Newman, The helicopter – efficiency or efficacy?, Aircr. Eng. Aerosp. Technol. 78 (1) (2006) 15–19. doi:10.1108/17488840610639636.

[25] W. Bao, W. Wang, X. Chen, H. Zhang, Q. Zhao, Numerical analyses of aeroacoustic characteristics of tiltrotor considering the aerodynamic

interaction by the fuselage in hover, Aerospace Science and Technology 141 (2023) 108558. doi:https://doi.org/10.1016/j.ast.2023.108558.

[26] L. A. Young, D. Lillie, M. McCluer, G. K. Yamauchi, Insights into Airframe Aerodynamics and Rotor-on-Wing Interactions from a 0.25-Scale Tiltrotor Wind Tunnel Model, Tech. rep., National Aeronautics and Space Administration Moffett Field CA AMES Research Center (2002).

[27] Full Report - Study on the societal acceptance of Urban Air Mobility in Europe (2023).
URL https://www.easa.europa.eu/en/full-report-study-societal-acceptance-urban-air-mobility-europe

[28] W. Rhee, L. Myers, D. McLaughlin, Aeroacoustics of Vertical Lift Ducted Rotors, in: 15th AIAA/CEAS Aeroacoustics Conference (30th AIAA Aeroacoustics Conference), 2012.
URL https://arc.aiaa.org/doi/abs/10.2514/6.2009-3333

[29] J. Sagaga, S. Lee, Acoustic Predictions for the Side-by-Side Air Taxi Rotor in Hover, 2021. doi:10.4050/F-0077-2021-16695.

[30] Fast-Forwarding to a Future of On-Demand Urban Air Transportation (2016).
URL https://uberpubpolicy.medium.com/fast-forwarding-to-a-future-of-on-demand-urban-air-transportation-f6ad36950ffa

[31] F. Yunus, D. Casalino, F. Avallone, D. Ragni, Efficient prediction of urban air mobility noise in a vertiport environment, Aerosp. Sci. Technol. 139 (2023) 108410. doi:10.1016/j.ast.2023.108410.

[32] M. Barbarino, F. Petrosino, A. Visingardi, A high-fidelity aeroacoustic simulation of a VTOL aircraft in an urban air mobility scenario, Aerosp. Sci. Technol. 125 (2022) 107104. doi:10.1016/j.ast.2021.107104.

[33] M. Rao, S. Biswas, B. Butz, D. Miller, Dynamic modeling and feedback control of a side-by-side tandem helicopter, in: Proceedings. 5th IEEE International Symposium on Intelligent Control 1990, Vol. 2, 1990, pp. 780–785. doi:10.1109/ISIC.1990.128546.

[34] C. Y. Huang, R. Celi, I. Shih, Reconfigurable Flight Control Systems for a Tandem Rotor Helicopter, J. Am. Helicopter Soc. 44 (1) (1999) 50–62. doi:10.4050/JAHS.44.50.

[35] P. D. Talbot, B. E. Tinling, W. A. Decker, R. T. N. Chen, A mathematical model of a single main rotor helicopter for piloted simulation, Tech. rep., nASA Ames Research Center, Document ID: 19830001781 (1982). URL `https://ntrs.nasa.gov/citations/19830001781`

[36] H. S. Choi, E. T. Kim, D. I. You, H. Shim, Improvements in Small-scale Helicopter Rotor Modeling for the Real-time Simulation of Hovering Flight, Trans. Jpn. Soc. Aeronaut. Space Sci. 54 (185+186) (2011) 229–237. doi:10.2322/tjsass.54.229.

[37] W. Johnson, Helicopter Theory, Courier Corporation, 2012.

[38] R. T. N. Chen, A simplified rotor system mathematical model for piloted flight dynamics simulation, Tech. rep., NASA Ames Research Center, Document ID: 19790015806 (1979).
URL https://ntrs.nasa.gov/citations/19790015806

[39] R. T. N. Chen, Effects of primary rotor parameters on flapping dynamics, Tech. rep., NASA Ames Research Center, Document ID: 19800006879 (1980).
URL https://ntrs.nasa.gov/citations/19800006879

[40] I. H. Abbott, A. E. V. Doenhoff, Theory of Wing Sections, Including a Summary of Airfoil Data, Dover Publications, 1959.

[41] L. A. Viterna, D. C. Janetzke, Theoretical and experimental power from large horizontal-axis wind turbines, Tech. rep., NASA Lewis Research Center, Cleveland, OH (United States) (1982). doi:10.2172/6763041.

[42] S. Taamallah, A flight dynamics helicopter UAV model for a single pitch lag flap main rotor, in: 36th Eurpean Rotorcraft forum, 2010, pp. 1–93.

[43] W. Kruger, On Wind Tunnel Tests and Computations Concerning the Problem of Shrouded Propellers, Tech. rep., nTRS Research Center: Headquarters (HQ), Document ID: 20050241797 (1949).
URL https://ntrs.nasa.gov/citations/20050241797

[44] J. G. Leishman, Principles of Helicopter Aerodynamics, Cambridge University Press, 2016.

[45] B. G. Jimenez, R. Singh, Effect of Duct-Rotor Aerodynamic Interactions on Blade Design for Hover and Axial Flight, in: 53rd AIAA Aerospace Sciences Meeting, American Institute of Aeronautics and Astronautics. URL https://arc.aiaa.org/doi/abs/10.2514/6.2015-1030

[46] A. I. Abrego, R. W. Bulaga, M. Rutkowski, Performance Study of a Ducted Fan System, Tech. rep., nTRS Research Center: Ames Research Center (ARC), Document ID: 20020052231 (2002).
URL https://ntrs.nasa.gov/citations/20020052231

[47] B. N. Bourtsev, S. V. Selemenev, Fan – in – Fin Performance at Hover Computational Method, in: European Rotorcraft Forum, 2000.

[48] J. Zhu, G. Xu, Y. Shi, An efficient method for helicopter fuselage shape optimization, Aircraft Engineering and Aerospace Technology 95 (7) (2023) 1069–1080. doi:10.1108/AEAT-06-2022-0152.

[49] J. Y. Hwang, M. K. Jung, O. J. Kwon, Numerical study of aerodynamic performance of a multirotor unmanned-aerial-vehicle configuration, Journal of Aircraft 52 (3) (2015) 839–846.

[50] G. Gibertini, F. Auteri, G. Campanardi, C. Macchi, A. Zanotti, A. Stabellini, Wind-tunnel tests of a tilt-rotor aircraft, The Aeronautical Journal 115 (1167) (2011) 315–322.

[51] G. D. Padfield, Helicopter Flight Dynamics: The Theory and Application of Flying Qualities and Simulation Modelling, John Wiley & Sons, 2008.